APS physics

CHORUS
Clearinghouse for the Open Research of the United States

This is the accepted manuscript made available via CHORUS, the article has been published as:

Local structure, pseudosymmetry, and phase transitions in Na_{1/2}Bi_{1/2}TiO_{3}–K_{1/2}Bi_{1/2}TiO_{3} ceramics

I. Levin, I. M. Reaney, E-M. Anton, Wook Jo, J. Rödel, J. Pokorny, L. A. Schmitt, H-J. Kleebe, M. Hinterstein, and J. L. Jones

Phys. Rev. B **87**, 024113 — Published 31 January 2013

DOI: 10.1103/PhysRevB.87.024113

Local Structure, Pseudo-Symmetry, and Phase Transitions in $Na_{½}Bi_{½}TiO_3$-$K_{½}Bi_{½}TiO_3$ Ceramics

I. Levin[1], I. M. Reaney[2], E-M. Anton[3], Wook Jo[3], J. Rödel[3], J. Pokorny[2], L. A. Schmitt[4], H-J. Kleebe[4], M. Hinterstein[5], J. L. Jones[6]

[1] Ceramics Division, National Institute of Standards and Technology, Gaithersburg MD 20899, USA
[2] Department of Engineering Materials, University of Sheffield, Sheffield, UK
[3] Department of Materials Science, Technische Universtität, Darmstadt 64287. Germany
[4] Institute of Applied Geosciences, Technische Universtität, Darmstadt 64287, Germany
[5] Institut für Werkstoffwissenschaft, Technische Universität Dresden, 01062 Dresden, Germany
[6] Department of Materials Science and Engineering, University of Florida, Gainesville, Florida 32611, USA

Abstract

The structural behavior of ceramic solid solutions $(1-x)Na_{½}Bi_{½}TiO_3$-$xK_{½}Bi_{½}TiO_3$ (NBT-KBT) was studied using high-resolution powder diffraction and transmission electron microscopy. A temperature-independent morphotropic phase boundary (MPB) separating NBT-like pseudo-rhombohedral (R) and KBT-like pseudo-tetragonal (T) phases was observed at $x \approx 0.2$. For $x<0.2$, both local and average room-temperature structures are similar to those in NBT. Simultaneous long-range anti-phase and short-range in-phase octahedral rotations average, resulting in effective anti-phase $a^-a^-c^-$ tilting, which yields monoclinic symmetry when probed by X-ray diffraction (XRD). For these compositions, polar ordering is coupled to anti-phase octahedral rotations so that tilting and ferroelectric (FE) domains coincide. Compositions with $x>0.2$ exhibit a tetragonal-like distortion; however, complex splitting of reflections in XRD patterns suggests that the actual symmetry is lower than tetragonal. For $0.2 \leq x \leq 0.5$, in-phase octahedral tilting $a^0b^+a^0$ (or $a^+b^0b^0$) is present but confined to the nanoscale, while for $x>0.5$, the structure becomes untilted. In-phase tilting evolves above the ferroelectric transition and occurs around a non-polar (*a* or *b*) axis of the average T structure. The onset of polar order has no significant effect on the coherence length of in-phase tilting, which suggests only weak coupling between the two phenomena. The average symmetry of the T phase is determined by the effective symmetry (*Imm2*) of assemblages of coherent in-phase tilted nanodomains. Near the MPB, the coexistence of extended R- and T-like regions is observed, but lattice distortions within each phase are small, yielding narrow peaks with a pseudo-cubic appearance in XRD. The temperature of the FE phase transition exhibits a minimum at the MPB. The structured diffuse scattering observed in electron diffraction patterns for all the compositions suggests that polar order in NBT-KBT solid solutions is modulated away from the average displacements refined using powder diffraction data.

Introduction

$Na_{½}Bi_{½}TiO_3$-based perovskite-like systems are promising lead-free alternatives to $Pb(Zr,Ti)O_3$ (PZT) piezoelectrics [1-4]. Typically, these materials are solid solutions (e.g. with $K_{½}Bi_{½}TiO_3$, $BaTiO_3$, $(K,Na)NbO_3$), which exhibit a morphotropic phase boundary yielding enhanced piezoelectric response. Numerous studies of crystal and domain structures in pure $Na_{½}Bi_{½}TiO_3$ (NBT) and various NBT-based solid solutions, including $Na_{½}Bi_{½}TiO_3$- $K_{½}Bi_{½}TiO_3$, have been reported [5-24]. The results revealed structural complexity which rivals that of PZT. Various aspects of atomic displacements, ensuing lattice distortions, and domain patterns have been highlighted but an overarching picture of the local and average structures in the NBT-based systems is still missing.

Early diffraction studies of NBT [5-7] suggested rhombohedral *R3c* symmetry with polar cation displacements and $a^-a^-a^-$ [22] anti-phase rotations of oxygen octahedra. More recent high-resolution X-ray diffraction measurements concluded that the actual symmetry of this phase is monoclinic *Cc*, which was attributed to $a^-a^-c^-$ tilting [12]. Transmission electron microscopy (TEM) revealed the co-existence of long-range anti-phase and short-range in-phase octahedral rotations [8-10, 22]. The local and average structures of NBT were reconciled with a model which assumed mesoscale aggregates of coherent nanoscale pseudo-orthorhombic domains with $a^-a^-c^+$ tilting, where the correlation length of the in-phase tilting was a few unit cells – much shorter than the correlation length of the anti-phase tilting [23]. These aggregates exhibit average $a^-a^-a^-$ or $a^-a^-c^-$ rotations, resulting in pseudo-rhombohedral symmetry revealed by X-ray diffraction. Unequal fractions of the three orthorhombic variants within the scattering volume were deemed responsible for the apparent monoclinic *Cc* symmetry. Electron diffraction indicated extensive diffuse scattering attributed to complex correlations among local cation displacements that remain partially disordered [23]. On heating, NBT undergoes a phase transition to a tetragonal structure which exhibits off-center cation displacements along the tetragonal axis combined with in-phase octahedral rotations that yield *P4bm* symmetry; the transition spans a broad temperature range [7]. Formation of the intermediate orthorhombic structure with long-range $a^-a^-c^+$ tilting also has been reported [9-10]. According to a model recently proposed by Levin and Reaney [23], the transitions are accompanied by changes of the coherence lengths of the competing in-phase and anti-phase tilting order parameters; the dominant order parameter exhibits a larger coherence length, which determines the average symmetry. In contrast to NBT, the structure of $K_{½}Bi_{½}TiO_3$ (KBT) is untilted (consistent with a larger ionic radius of K relative to Na) and exhibits tetragonal *P4mm* symmetry with polar cation displacements [24].

The (1-*x*)NBT-*x*KBT phase diagram features a morphotropic phase boundary (MPB) at *x*=0.2 which separates the NBT-rich pseudo-rhombohedral (R) and KBT-rich tetragonal (T) phases [15].

This boundary occurs at $x \approx 0.2$ for the NBT-KBT ceramics. The Curie temperature reportedly exhibits a minimum at the MPB [15]. Pronin *et al.* suggested the existence of a pseudo-cubic ferroelectric phase for $0.18<x<0.4$, which is sandwiched between rhombohedral and tetragonal phase fields [15]. Other reports [15] indicated a mixture of the R and T structures in the vicinity of the MPB. However, diffraction evidence presented in all of these studies is limited and unconvincing. According to recent TEM studies of ceramic samples [20], compositions with $x<0.2$ exhibit long-range anti-phase tilting ($a^-a^-a^-$), whereas for $x>0.2$ in-phase tilting dominates. The $x=0.2$ sample was found to be predominantly tetragonal with in-phase tilting [20]. Reflection-splitting in electron diffraction patterns from the twin assemblages in the tetragonal structure [20] suggested that the in-phase tilting occurs around one or both of the *non-polar* axes. This observation conflicts with the structural model for the high-temperature tetragonal phase in NBT, where in-phase tilting occurs about the *polar c*-axis; however, no discussion of this apparent discrepancy has been presented.

Despite numerous studies, several important questions regarding the structural and domain state at the MPB as well as the crossover between the local and average structure of the tetragonal NBT-KBT phase remain unclear. The outstanding issues include the relationship between directions of the tilting axes and polar cation displacements, the coherence length of the in-phase tilting relative to that of the cation displacements, and the occurrence of cation displacive disorder as identified in NBT. In the present study, we combine high-resolution synchrotron X-ray diffraction with conventional and high-resolution TEM to address these questions and obtain new insights into the structural behavior of the NBT-KBT system.

Experimental

A series of (1-*x*)NBT-xKBT (x=0, 0.1, 0.15, 0.175, 0.2, 0.225, 0.25, 0.3, 0.4, 0.5, 0.6) specimens were prepared using solid state synthesis. Powders of Bi_2O_3 (99.975 %), Na_2CO_3 (99.5 %), K_2CO_3 (99.0 %) and TiO_2 (99.9 %) were mixed and planetary-milled (Fritsch [25], Germany) at 250 rpm in ethanol using zirconia grinding media for 24 h. Hygroscopic K_2CO_3 was weighed in a dry argon atmosphere in a glove box. Milled powders were dried, ground, and calcined in covered alumina crucibles at 800 °C for 5 h (heating rate of 5 °C/min). The calcined powders were re-milled under the same conditions as used for the raw powder mixture. Subsequently, the powders were pelletized using cold isostatic pressing at 350 MPa and sintered in covered alumina crucibles at 1080 °C for 3 h. The pellets (7 mm in diameter and ≈1.4 mm thick) were embedded in powder of the same composition to prevent possible evaporation of volatile species during sintering.

Samples were characterized using both laboratory and synchrotron-radiation powder diffractometers. A Panalytical X'Pert Pro laboratory diffractometer was configured with an incident-beam monochromator (Cu $K_{\alpha 1}$), position sensitive detector, and an Anton Paar heating

stage HTK-16. For variable-temperature measurements, sample powders obtained by crushing sintered pellets were dispersed in ethanol and deposited on a platinum heater. Prior to the measurements, all samples were annealed at 400 °C for 30 min (in the HTK-16 chamber) to mitigate residual stresses. As demonstrated previously [23], this annealing is critical because residual stresses have marked effects on average lattice distortion. Similar effects of residual stresses were observed for the present solid-solution samples. Synchrotron-radiation studies were performed at beamline 11-BM (λ=0.41396 Å) of the Advanced Photon Source at Argonne National Laboratory. Prior to these measurements, powder samples were annealed at 400 °C for 1 h in closed alumina crucibles. For synchrotron measurements, the powder was loosely packed in quartz capillaries (diameter 0.7 mm), which were spun at 60 Hz during measurements to improve crystallite averaging. A scintillator-based multicrystal analyzer detector was used to record the signal. A hot gas blower was used for variable-temperature measurements between room temperature and 500 °C. Rietveld refinements were completed using the software package FullProf [26].

TEM samples were prepared by mechanical sectioning and polishing followed by dimpling to a thickness of 30 μm. The thinning was completed using Ar ion milling (4.5 kV, 4.5 °) until perforation. The samples were coated with a thin layer of carbon to prevent electric charging prior to inserting them into an electron microscope. Selected samples were annealed after dimpling and prior to ion-thinning to eliminate residual stresses. A Philips CM-30 (200 kV) and an FEI Titan (300 kV) microscopes were used for conventional and high-resolution TEM, respectively.

Variable-temperature dielectric capacitance and loss-factor were measured using *unpoled* sintered pellets (less than 1 mm thick) sputter-coated with silver electrodes. An HP LCR meter (4284A) and a Nabertherm furnace were used. A heating rate was 2 K/min. Dielectric permittivity was calculated from the capacitance values.

Results and Discussion

X-ray Diffraction

X-ray diffraction for $x<0.2$ (Fig. 1) reveals non-split 200 and split 110 and 111 reflections, consistent with pseudo-R symmetry. (Hereafter, all reflections are indexed according to a pseudocubic perovskite unit cell, $a\approx4$ Å.) The 110 reflection is split into at least three peaks (note well-defined shoulders for this peak in NBT) indicating symmetry lower than rhombohedral. For $x=0.2$, the 200 and 111 peaks exhibit a weak shoulder on the low d-spacing side, whereas the 110 peak is flanked by weak shoulders on both sides. The presence of these shoulders becomes evident only when the patterns are displayed on the square-root or logarithmic scales; otherwise, the structure appears to be cubic. For $x>0.2$, the 200 peak is

split, whereas both 111 (apart for x=0.3) and 110 reflections appear as single, albeit broad, peaks, which concurs with a tetragonal-like distortion. However, the 200 peak is split into at least three components, suggesting symmetry lower than tetragonal. The superlattice reflection ½311, associated with anti-phase tilting, remains visible for $x<0.20$ but disappears for higher x-values; no superlattice reflections are observed for $x\geq0.2$.

As expected from the complex peak splitting (Fig. 1), Rietveld refinements (not shown) using single rhombohedral/monoclinic or tetragonal phases for $x<0.2$ and $x>0.2$, respectively, yielded unsatisfactory fits. However, a significant improvement was obtained by introducing an additional cubic (C) phase and using two-phase mixtures (R + C) and (T + C) to fit the data for $x<0.2$ and $x>0.2$, respectively. For $x=0.2$, a three-phase mixture (R+T+C) was used. A refined fraction (f) of the cubic phase $f\approx0.4$ remained approximately constant across the composition range studied (x<0.6), apart from $x=0.2$ for which $f=0.9$. Likely, this cubic phase compensates for local deviations from the rhombohedral and tetragonal symmetries, as discussed below. A pseudo-cubic appearance of the structure at the MPB is consistent with an earlier report [16].

Transmission electron microscopy

Pseudo-Rhombohedral Phase Field (x<0.2)

Figure 2 summarizes ⟨310⟩ electron diffraction patterns for a series of NBT-KBT compositions. Samples with $x<0.2$ exhibit sharp ½{*ooo*} and diffuse ½{*ooe*} superlattice reflections similar to those in NBT (hereafter, "*o*" and "*e*" refer to odd and even reflection indexes, respectively). In the $x=0.1$ sample, many grains are devoid of twin boundaries while featuring large anti-phase domains typical for $a^-a^-a^-$-type tilting (Fig. 3). The twin domains observed in dark-field images of these samples represent crystallographic variants of the pseudo-R structure (Fig. 3). The domain boundaries reside on {100} and {110} planes (Fig. 3b, 4a), which are known to provide strain accommodation in a rhombohedral structure. High-resolution TEM images (not shown) of the $x<0.2$ samples Fourier-filtered using diffuse ½{*ooe*} reflections revealed a nanoscale domain texture associated with a short-range in-phase tilting, similar to that observed in NBT [23]. Occasional regions in the $x=0.15$ sample featured well-defined ½{*ooe*} reflections (Fig. 4b-d), which were associated with nanoscale domains typical for the in-phase tilted tetragonal-like structure described below; presumably, the presence of these regions reflects compositional fluctuations. The interfaces between the R and T-type regions, while likely being coherent, are irregular without any preferred crystallographic orientation.

Electron diffraction patterns from $x<0.2$ samples exhibit structured diffuse scattering [27], which corresponds to traces of $\{111\}^*$ (asterisk indicates reciprocal space) and $\{100\}^*$ diffuse sheets, similar to those encountered in NBT [23]. This diffuse scattering was attributed to the local cation ⟨111⟩ displacements correlated along both ⟨111⟩ and ⟨100⟩ directions [23].

Morphotropic Phase Boundary (x=0.2)

In the *x*=0.2 sample, ½{*ooe*} reflections (Fig. 5a) caused by in-phase tilting become dominant but many areas still produce additional ½{*ooo*} spots. Dark-field imaging (Fig. 5) demonstrates that ½{*ooe*} reflections, which appear streaked along ⟨100⟩ directions, are associated with ⟨100⟩-textured nanoscale domains, whereas round-shaped ½{*ooo*} reflections always correspond to anti-phase domains, tens of nanometers in size (Fig. 5b). In many areas, both superstructures coexist in the same grain with the anti-phase-tilted regions located in the grain periphery, while occasional grains feature exclusively ½{*ooo*} reflections and large anti-phase domains. Overall, the pseudo-R and T phases coexist as separate extended regions (similar to the area imaged in Fig. 4) rather than a nanoscale mixture. Considering the presence of occasional T regions even in the *x*=0.15 sample, the coexistence of phases for *x*=0.2 also likely reflects compositional fluctuations rather than the equilibrium. Many grains with ½{*ooe*} reflections exhibit twins typical for a tetragonal structure whereas others either contain irregular twin domains or appear as twin-free. XRD indicates that the average distortions in both R- and T-like phases at this composition are small, as expected at an MPB where polar anisotropy vanishes [28].

Pseudo-tetragonal Phase Field (x>0.2)

For *x*>0.2, ½{*ooe*} reflections streaked along ⟨100⟩ directions dominate, while ½{*ooo*} reflections weaken drastically (Fig. 2). For *x*=0.5, even ½{*ooe*} reflections nearly disappear (Fig. 2). The structured NBT-like diffuse scattering due to local modulations of cation displacements is retained for the tetragonal compositions (Fig. 6). Very weak and diffuse 1/2{*ooo*} spots are attributed to enhanced intensity at the intersection of 2 or 3 (dependent on the number of variants) ⟨100⟩ diffuse rods (see reciprocal lattices in Fig. 2, Fig. 6).

Samples with *x*>0.2 display well-defined twin domains (hereafter referred to as **T1** domains), a few tens of nanometers thick, separated by interfaces predominantly parallel to {110} planes (Fig. 7). These domains are consistent with the average tetragonal-like distortion identified using X-ray diffraction (The sensitivity of domain structure to the electron beam varied from grain to grain but in many cases no noticeable effects were observed.). Some grains appear devoid of domain boundaries whereas others feature complex domain patterns. Frequently, twin boundaries concentrate at the periphery of a grain. The majority of 90°-domain walls in the present TEM foils is of the *a*-*c* type when viewed along ⟨100⟩ directions. Overall, the domain structures in the present tetragonal samples appear to be less regular than those reported by Otoniĉar *et al.* [20]. Likely, these differences reflect the effects of TEM sample preparation and the associated level and distribution of residual stresses.

Dark-field imaging using ½{*ooe*} reflections (Fig. 8) highlights a nanoscale {100} domain texture (similar to that observed in the *x*=0.2 sample, Fig. 5a), within the T1 domains; the size of these nanodomains is ≈5 nm. Imaging the same area using, for example, ½310 and ½013 reflections suggests that each T1 domain contains at least two nanoscale rotational variants (**T2** domains) associated with ½{*ooe*} spots (Fig. 8). In most cases, the Fast Fourier Transform (FFT) of phase contrast in the ⟨111⟩ HRTEM images reveals two sets of similar-intensity ½{*ooe*} reflections, whereas the third set is nearly absent (Fig. 9). Filtering these images using ½{*ooe*} frequencies further indicates that a given region consists of a mixture of T2 domains rather than a single domain, consistent with dark-field images (Fig. 9). FFT patterns and ⟨111⟩ selected area electron diffraction patterns from some grains revealed no obvious changes in the type and number of T2 variants across the T1 twin boundaries viewed edge-on (Fig. 10), thereby suggesting the absence of a well-defined orientation relationship between the average tetragonal axis and the in-phase tilting axis. Yet, in other grains at least one of the three T2 variants in a given T1 domain appeared to be missing (not shown here). This latter result concurs with a previous inference of the untilted *c*-axis in the T1 domains based on different splitting of ½{*ooe*} reflections across the *a*-*a* and *a*-*c* domain walls [20].

The reasons for such grain-to-grain variations remain uncertain, but the results support *in-phase* octahedral tilting about the *non-polar* axis of the average "tetragonal" structure. In NBT, the high-temperature tetragonal phase is described by a superposition of *in-phase* (i.e. $a^0a^0c^+$) octahedral rotations and cation displacements that yield tetragonal *P4bm* symmetry; both the tilting axis and cation displacements are aligned with the tetragonal [001] direction. Following the notation by Stokes *et al*. [29], an overall displacement pattern in the tetragonal phase of NBT can be described as $a^0b^0c^+_+$. In contrast, our results for the "tetragonal" NBT-KBT compositions suggest an $a^+b^0c^0_+$-type model. This model yields orthorhombic *Amm2* symmetry [29] with $a=a_c$, $b\approx 2a_c$, $c=2a_c$ (where a_c=4 Å is the lattice parameter of an ideal cubic perovskite structure).

From our observations, a single T1 domain in the NBT-KBT samples is an agglomerate of coherent nanoscale T2 domains with $a^+b^0b^0$ and $a^0b^+a^0$ tilting, which in the absence of cation displacements would yield *P4/mbm* symmetry within the T2 nanodomains. The reciprocal lattice of this agglomerate (assuming equal fractions of inequivalent ½{*ooe*} variants) can be described using *I4/mmm* pseudo-symmetry, which corresponds to pseudo $a^+a^+c^0$ tilting with $a=2a_c$, $c=2a_c$; however, each octahedron still rotates about a *single* four-fold symmetry axis [30]. For a two-domain mixture, a pseudo-tetragonal axis of the agglomerate (i.e. a T1 domain) coincides with a zero-tilt direction.

The macroscopic tetragonal distortion in the NBT-KBT system (and formation of T1 domains) is associated with cation off-centering along the *c*-axis as it occurs in KBT. Structured diffuse

scattering encountered across the entire compositional range studied is attributed to ⟨111⟩-like cation displacements correlated along ⟨111⟩ and ⟨100⟩ directions [25]; that is, NBT-KBT solid solutions exhibit considerable cation displacive disorder with *partial* polar order manifested in the average displacements/distortions identified using powder diffraction and in the appearance of extended T1 twin domains. Additionally, regions having different local compositions because of heterogeneous A-cation distributions can exhibit distinct directions of the A-cations displacements [31].

The most symmetric configuration that combines in-phase tilting about two axes (*I4/mmm* symmetry) with the tetragonal distortion of KBT (*P4mm* symmetry) would exhibit average cation displacements directed along the zero-tilt axis, thereby yielding *I4mm* symmetry [29]. In this case, tetragonal distortion due to cation displacements can be expected to only weakly affect the underlying octahedral tilting. A combination of the three-axis equal-magnitude in-phase tilting and tetragonal distortion also yields *I4mm* space group symmetry [29]. Deviations of tilted-domain fractions from their random values will reduce the overall pseudo-symmetry to orthorhombic *Imm2* or lower [29]. These deviations likely occur in the NBT-KBT solid solutions as reflected by the complex peak splitting in XRD patterns, which cannot be described by tetragonal distortion. Conceivably, large tetragonal distortion favors oxygen displacements along the *c*-axis, which is the case for the $a^+b^0b^0$ and $a^0b^+a^0$ tilting patterns, but not for the $a^0a^0c^+$ tilting, where oxygen displacements are confined to the *a*-*b* plane.

Variable-temperature TEM experiments demonstrate that ½{*ooe*} reflections persist above the temperature of disappearance of the T1 domains (Fig. 11); that is, octahedral tilting develops prior to polar ordering with decreasing temperature. These reflections strengthen and sharpen on cooling but remain diffuse down to at least -170 °C, with the corresponding in-phase tilting still limited to the nanoscale. In contrast, the average cation displacements become coherent over distances ranging from tens to hundreds (single-domain grains) of nanometers as manifested in the size of the T1 domains and resolvable 200 and 110 peak splitting in X-ray diffraction. Such distinct coherence lengths for the in-phase ($a^0b^+a^0$ or $a^+b^0b^0$) octahedral rotations and average polar displacements suggest that the coupling between the two types of ordering is weak. This behavior differs from that observed for the high-temperature tetragonal polymorph of NBT, where both tilting and polar ordering exhibit similar coherence lengths, large enough to be clearly observable in XRD patterns. Likewise, a*nti-phase* ($a^-a^-a^-$) octahedral rotations and polar ordering are coupled strongly in the pseudo-rhombohedral phase field (x<0.2), as manifested in the coincident tilting and ferroelectric domains.

Phase Transitions and Dielectric Anomalies

Figure 12 presents a diffusionless phase diagram for the NBT-KBT system with both local and average displacement patterns indicated in different phase fields. The transition temperatures

(T_0) to the cubic (as seen by XRD) structure were determined from the reflection splitting in XRD and the appearance of superlattice reflections in both XRD (if detectable) and electron diffraction. Considering small lattice distortions and complex peak splitting, the transition temperatures were estimated from variable-temperature measurements of the widths of those XRD reflections that could be fitted using a Pearson VII single-peak function; however, the behavior of other significant peaks was also monitored. The T_0 values were determined by fitting the temperature dependence (Fig. 13) of full-width-at half-maximum (FWHM) with a sigmoidal function $f(T)=\{A_1 + (A_1-A_2)/(1+\exp(T-T_0)/\Delta T)\}$, where A_1 and A_2 are asymptotic values of FWHM at low and high temperatures, respectively, T_0 corresponds to $(A_1+A_2)/2$, and ΔT characterizes the spread of the transition. This approach yields T_0 values that are lower than those determined from the onset of lattice distortion with the difference depending on the spread of the transition; however, sigmoidal fits enable robust comparison of the T_0 trends with composition while also providing ΔT values. For KBT, the T_0 value quoted on the diagram was obtained by fitting a sigmoidal function to the temperature dependence of the *c*/a ratio reported in Ref. [21].

For NBT, no anomalies in the widths of 110 and 200 peaks were observed up to an abrupt transition to the high-temperature tetragonal polymorph at ≈280 °C (Fig. 14). The transitions to the pseudo-cubic structure appear to be abrupt for $x<0.2$ and continuous for $x\geq0.2$. The ΔT-values on the rhombohedral side are a factor of ≈3 smaller than those on the tetragonal side; the character and temperature-spread of the transition change abruptly across the MPB (Fig. 14). A small hysteresis is observed between heating and cooling (Fig. 13) suggesting that these transitions are first-order (2 heating/cooling cycles were performed for each sample to confirm reversibility). The behavior of peak widths at the MPB does not follow a sigmoidal dependence. Here, T_0 can be determined from the anomaly in the slope of the peak-width dependence on temperature. The T_0 for the transition to the pseudocubic structure exhibits a well-defined minimum at the MPB (Fig. 12), in agreement with Ref. [17].

The temperatures for the in-phase tilting transition, which, apart for NBT, are estimated from the TEM data, should be viewed as approximate. Considering the very low intensity and diffuse appearance of the ½{*ooe*} reflections for $x=0.5$, the tilting phase transition for this composition is assumed to occur near room temperature. The coherence length for the in-phase tilting is reduced from long-range for NBT to the nanoscale range for the NBT-KBT compositions, as inferred from the absence of ½{*ooe*} superlattice reflections in the synchrotron XRD data for $x=0.1$ (the lowest KBT concentration studied), while these reflections are visible in NBT.

For the solid-solution samples with $x\geq0.1$, the temperatures of the transitions to the cubic (or pseudo-cubic) state derived using X-ray diffraction agree reasonably with the lower-temperature dielectric anomaly (labeled using a gray dashed line in Fig. 15, $x=0.1$), which has

been identified with a ferroelectric (FE) transition [15]. The characteristic temperature for the dielectric anomaly (open green circles in Fig. 12) was estimated from the maximum in the first derivative of the real part of permittivity, as described in Ref. [32]. Previously, this temperature was shown to be about 5 °C to 20 °C higher than the depolarization temperature, defined as the steepest decrease in remnant polarization [32]. For unpoled NBT, the dielectric anomaly is rather broad and the inflection point occurs near ≈162 °C which is well below the R↔T transition (≈280 °C). Poling of NBT sharpens this anomaly considerably [16, 33] raising the inflection point to ≈170 °C. The temperature of the dielectric anomaly increases from ≈160 °C/170 °C for NBT to 195 °C for x=0.1 and then decreases for 0.1<x<0.2. For 0.1≤x<0.2, the temperatures of the tilting and FE transitions coincide within the resolution of the present measurements. In the solid-solution samples, the dielectric anomaly appears sharp for 0.1≤x<0.2 and much broader for x>0.2, which agrees with the ΔT values observed for the corresponding compositional ranges (Fig. 13).

Our results support existence of a non-FE phase with the average anti-phase tilting ($a^-a^-a^-$ or $a^-a^-c^-$) which, in NBT, is stable approximately between 280 °C and 170 °C. Below 170 °C, the polar displacements become ordered yielding a FE phase with the average tilting- and polar-ordering pattern described as $a_+^-a_+^-c_+^-$. This intermediate-phase field (delimited by the black solid and green dashed lines in Fig. 12) shrinks rapidly with KBT substitution and disappears for x≥0.1. Further studies of the solid solutions with x<0.1 are warranted to clarify phase transitions in this concentration range.

The minimum of the FE transition temperature at the MPB in NBT-KBT solid solutions contrasts with the monotonic behavior of the Curie temperature in PZT. In PZT, Ti off-centering contributes strongly to polarization and the Curie temperature tracks the concentration of Ti across the diagram. The perovskite tolerance factor increases with Ti substitution so that octahedral tilting becomes suppressed; however, the onset of octahedral tilting in PZT occurs well below the FE transition. In NBT-KBT, the main contribution to polarization comes from Bi displacements, as can be inferred from the much larger magnitude of Bi off-centering relative to that of Ti [7, 17, 21]. The concentrations of both FE-active ions (Bi and Ti) are fixed across the diagram. The perovskite tolerance factor increases with increasing concentration of potassium and octahedral tilting is suppressed. Considering that tilting affects Bi-O distances, strong interactions between octahedral rotations and polar Bi displacements are expected. In the *R3c* (or *Cc*) phase, tilting and polarization are strongly coupled but at the MPB (x>0.2), the FE instability becomes decoupled from tilting, which may account for the gradual increase in the FE-transition temperature in the T-like phase as potassium concentration increases.

Summary

Our results demonstrate that similar to NBT, (1-*x*)NBT-*x*KBT solid solutions exhibit pseudo-symmetries determined by the interplay of the coherence lengths of octahedral rotations and ordered cation displacements. Potassium substitution in NBT gradually suppresses octahedral tilting as expected from tolerance-factor considerations. For $x<0.2$, the structure remains similar to NBT with a pseudo-rhombohedral distortion associated with anti-phase/in-phase octahedral rotations and cation displacements. Anti-phase rotations are strongly coupled to polar cation ordering so that tilting and ferroelectric domain-walls coincide. For $x>0.2$, only the in-phase rotations survive but remain limited to the nanoscale regardless of composition down to low temperatures. In contrast, cation displacements become ordered over a long range with the corresponding lattice distortion detectable in X-ray diffraction. Ordering of cation displacements occurs at temperatures below the onset of in-phase octahedral tilting without any significant effect on the size of tilted domains which remain confined to the nanoscale at least down to 100 K. Thus, in-phase octahedral tilting appears to be weakly coupled to ferroelectric cation displacements. The local symmetry of the tetragonal phase is proposed as *Amm2* ($a=a_c$, $b\approx 2a_c$, $c=2a_c$), but the average symmetry for the assemblages of the in-phase-tilted nanodomains can be approximated as *I4mm* ($a=2a_c$, $c=2a_c$) or *Imm2* ($2a=a_c$, $b\approx 2a_c$, $c=2a_c$); in fact, complex splitting of 100-type reflections in X-ray diffraction supports orthorhombic (or even lower) symmetry. The pseudo-tetragonal phase encountered in the NBT-KBT solid solutions differs from the high-temperature tetragonal phase of NBT by the relationship between the directions of polar cation displacements and the in-phase tilting axis. At the MPB, the rhombohedral- and tetragonal-like phases coexist as separate extended regions. The lattice distortions of both phases at the boundary are small, yielding narrow peaks with a pseudo-cubic appearance in X-ray diffraction patterns. Unlike some other MPB systems [28], no miniaturization of ferroelectric non-180° domains is observed near the MPB.

Acknowledgements

This work benefited from the use of the Advanced Photon Source supported by the Department of Energy Office of Basic Energy Sciences under Contract No DE-AC02-06CH11357. The assistance of Matthew Suchomel, Benjamin Kowalski, and Robert Dittmer in the measurements carried out at the APS is gratefully acknowledged. JJ acknowledges funding support from the U.S. National Science Foundation under award number DMR-0746902 and the U.S. Department of the Army under contract number W911NF-09-1-0435. Contributions by the Institute of Materials Science at Darmstadt were supported through the state center ADRIA.

References

1. T. R. Shrout and S. Z. Zhang, J. Electroceram., 19 [1] 113-126 (2007)
2. T. Takenaka, H. Nagata, and Y. Hiruma, Jpn. J. Appl. Phys., 47 [5] 3787-3801 (2008)
3. E. Aksel and J. L. Jones, Sensors, 10 [3] 1935-1954 (2010)
4. J. Rodel, W. Jo, K. T. P. Seifert, E.-M. Anton, T. Granzow, and D. Damjanovic, J. Am. Ceram. Soc., 92 [6] 1153-1177 (2009)
5. S. B. Vakhrushev, B. G. Ivanitskii, B. E. Kvyatkovskii, A. N. Maistrenko, R. S. Malysheva, N. M. Okuneva, and N. N. Parfenova, Sov. Phys. Solid State, 25 [9] 1504-1506 (1983)
6. S. B. Vakhrushev, V. A. Isupov, B. E. Kvyatkovskii, N. M. Okuneva, I. P. Pronin, G. A. Smolensky, and P. P. Syrnikov, Ferroelectrics, 63 [1-4] 153-160 (1985)
7. G. O. Jones and P. A. Thomas, Acta Cryst. B., 58, 168-178 (2002)
8. V. Dorcet and G. Trolliard, Acta Mater., 56 [8], 1753-1761 (2008)
9. V. Dorcet, G. Trolliard, and P. Boulay, Chem. Mater., 20 [15], 5061-5073
10. G. Trolliard and V. Dorcet, Chem. Mater., 20 [15], 5074-5082 (2008)
11. S. Gorfman and P. A. Thomas, J. Appl. Cryst., 43, 1409-1414 (2010)
12. E. Aksel, J. S. Forrester, J. L. Jones, P. A. Thomas, K. Page, and M. R. Suchomel, Appl. Phys. Lett., 98, 152901 (2011)
13. V. A. Shuvaeva, D. Zekria, A. M. Glazer, Q. Jiang, S. M. Weber, P. Bhattacharya, and P. A. Thomas, Phys. Rev. B., 71 [17] (2005)
14. O. Elkechai, M. Manier, and J. P. Mercurio, Phys. Status Solidi A, 157 [2], 499-506 (1996)
15. T. Takenaka, K. Maruyama, and K. Sakata, Jpn. J. Appl. Phys., Part 1, 30 [9B] 2236-2239 (1991)
16. I. P. Pronin, N. N. Parfenova, N. V. Zaitseva, V. A. Isupov, and G. A. Smolensky, Sov. Phys. Solid State, 24, 1060-1062 (1982)
17. G. O. Jones, J. Kreisel, and P. A. Thomas, Powder Diffr., 17 [4], 301-319 (2002)
18. V. A. Isupov, Ferroelectrics, 315, 123-147 (2005)
19. W. Zhao, H. P. Zhou, Y. K. Yan, and D. Liu, Key Eng. Mater., 368-372, 1908-1910 (2008)
20. M. Otonicar, S. D. Skapin, B. Jancar, IEEE Trans. Ultrason., Ferroelect. Freq. Control 58, 1928 (2011)
21. I. Jeong, C. Y. Park, D. J. Kim, S. –H. Kim, B. K. Moon, I. W. Kim, C. W. Ahn, Z. Krist., 226, 150 (2011)
22. A. M. Glazer, Acta Cryst. B.28, 3384 (1972)
23. I. Levin and I. M. Reaney, Adv. Funct. Mater., 22 [16], 3445-3452 (2012)
24. G. A. Smolenskii, V. A. Isupov, A. I. Agranovskaya, and N. N. Krainik, Sov. Phys. Solid State, 2, 2651 (1961)

25. Certain commercial equipment is identified in order to specify adequately the experimental procedure; recommendation or endorsement by the National Institute of Standards and Technology is not therein implied.
26. T. Roisnel, J. Rodriguez-Carvajal, Mater. Sci. Forum, 118 (378), 2001
27. G. Honjo, S. Kodera, N. Kitamura, J. Phys. Soc. Japan, 19 (3) (1964)
28. A. G. Khachaturyan, Phil. Mag., 90 [1-4], 37-60 (2012)
29. H. Stokes, E. H. Kisi, D. M. Hatch, and C. J. Howard, Acta Cryst. B, 58, 934-938 (2002)
30. In case of a three-domain mixture, the pseudo symmetry would be either cubic *Im-3* (i.e. $a^+a^+a^+$, equal domain fractions) or orthorhombic *Immm* ($a^+b^+c^+$) unequal domain fractions. A two-domain mixture with unequal domain fractions would yield pseudo symmetry *Immm* ($a^+b^+c^0$).
31. J. Kreisel, P. Bouvier, B. Dkhil, P. A. Thomas, A. M. Glazer, T. R. Welberry, B. Chaabane, and M. Mezouar, Phys. Rev. B., 68, 014113 (2003)
32. E-M. Anton, W. Jo, D. Damjanovic, and J. R□del, J. Appl. Phys., 110, 094108 (2011)
33. E. Aksel, J. S. Forrester, B. Kowalski, M. Deluca, D. Damjanovic, J. L. Jones, Phys. Rev. B., 85, 024121 (2012

Figure captions

Fig. 1: Traces of 200, 111, and 110, X-ray diffraction reflections (synchrotron data) for several (1-*x*)NBT-*x*KBT compositions. Peak splitting is consistent with pseudo-rhombohedral and pseudo-tetragonal symmetries for $x<0.2$ and $x>0.2$, respectively. The profiles for $x=0.1$ are similar to those for $x=0$ and therefore were omitted from this figure. The lattice distortion is minimal at the MPB ($x=0.2$), which creates the appearance of a cubic structure.

Fig. 2: Representative ⟨310⟩ selected area electron diffraction patterns for a series of (1-*x*)NBT-*x*KBT compositions. The superlattice reflections change from ½{*ooo*} for $x<0.2$ to ½{*ooe*} for $x>0.2$. For $x=0.2$, both types of reflections are present though the dominant type varies from grain to grain. For $x<0.2$, the diffuse spots at ½{*ooo*}, which are streaked along ⟨100⟩ directions, signify short-range ordered in-phase tilting. In contrast, for $x\geq0.2$, the round-shaped diffuse spots at ½{*ooo*} arise from intersections of several ⟨100⟩ diffuse rods associated with ½{*ooe*} reflections, as discussed in the text. The reciprocal lattices for both cases are illustrated in the figure.

Fig. 3: (a) A dark field image of a single grain, $x=0.1$, reveals anti-phase domain boundaries associated with octahedral tilting. (b) A dark-field image of another single grain in the same sample, which features both twin and anti-phase domain boundaries. The twin boundaries reside largely on {100} planes. Both images were recorded with ½{*ooo*} reflections strongly excited near the ⟨310⟩ orientation.

Fig. 4: Dark-field images (a, b) of a single grain, $x=0.15$, which exhibits a coexistence of regions that feature strong ½{*ooo*} and weak ½{*ooe*} superlattice reflections, as indicated in the corresponding selected area electron diffraction pattern (c). These images were recorded using ½{*ooo*} (a) and ½{*ooe*} (b) reflections strongly excited near the ⟨310⟩ zone-axis orientation. Image (a) reveals a twin-domain structure typical for a pseudo-rhombohedral structure with domain interfaces on both {100} and {110} planes. In fact, most grains in this sample exhibited exclusively ½{*ooo*} reflections with a similar twin-domain structure. Image (b) highlights an area with a nanoscale domain texture that is typical for a pseudo-tetragonal phase encountered for $x>0.2$. An interface between the R- and T-like phases is irregular without any obvious crystallographic orientation; yet, this interface is likely to be coherent. Image (d) is a superposition of the images (a) and (b) obtained using an overlay feature in Photoshop.

Fig. 5: Representative dark-field images (a, b) and the corresponding selected area electron diffraction patterns recorded from single grains, in $x=0.2$. Image (a), which was obtained using a ½310-type reflection (c) reveals a ⟨100⟩ nanoscale domain texture

typical for the pseudo-tetragonal phase. Image (b), recorded using ½{*ooo*} reflections (d), highlights relatively large anti-phase domains typical for a pseudo-rhombohedral structure with anti-phase octahedral tilting. Some grains exclusively exhibit one structure or another, whereas other grains contain both phases separated by irregular interfaces as imaged in Fig. 2.

Fig. 6: Representative selected area electron diffraction patterns, x=0.3, which exhibit well-structured diffuse scattering similar to that observed in NBT. The diffuse scattering contours are interpreted as traces of $\{111\}^*$ and $\{100\}^*$ diffuse sheets. Significant enhancement of diffuse intensity at the intersections of these traces is observed. All patterns display ½{*ooe*} superlattice reflections. The diffuse spots at ½{*ooo*} locations seen in [130] orientation arise from intersection of this reciprocal-lattice section with ⟨100⟩ diffuse rods (Fig. 2), as inferred from the presence of other characteristic extra spots (indicated using white arrows) and streaking of ½{*ooo*} spots (circled).

Fig. 7: Many-beam bright-field images of typical twin domain structures in samples with x>0.2

Fig. 8: A pair of dark-field images of the same area in a single grain, x=0.3, recorded using ½310 and ½301 reflections. The domains are textured along [001] (a) and [010] (b) directions. These images confirm that the same area contains at least two of the domain variants associated with ½{*ooe*} reflections.

Fig. 9: A colored overlay of the two ⟨111⟩ HRTEM images of the same T1 domain (x=0.3), each obtained by Fourier filtering a raw image using a distinct set of ½110-type reflections visible in the FFT pattern (inset). A given set of these superlattice reflections corresponds to one of the two domains (red or blue), which appear as spatially separate regions.

Fig. 10: A bright-field image and the corresponding ⟨111⟩ zone-axis electron diffraction pattern (x=0.3) recorded from a single T1 domain (circle 1), x=0.3. The diffraction pattern exhibits two variants of superlattice reflections; the third variant is missing. No changes in the orientation and number of variants were observed by recording a diffraction pattern from the area that encompassed two adjacent T1 domains (circle 2).

Fig. 11: ⟨310⟩ zone-axis patterns recorded from a single grain, x=0.4, at (a) room temperature and 100°C (b) and 150 °C (c) above the temperature of disappearance of the T1 domains. The ½{*ooe*} reflections still remain visible after the T1 domains disappear, even though the correlation length of the underlying in-phase tilting becomes significantly reduced relative to the room temperature structure.

Fig. 12: A diffusionless phase diagram for the (1-*x*)NBT-*x*KBT system determined from XRD, TEM measurements, and dielectric measurements. The asterisks (orange) represent experimental points determined from the XRD/TEM data, whereas open (green) circles correspond to the temperatures of the FE anomaly estimated from the dielectric data. Octahedral tilting and ferroelectric displacements in different phase fields are indicated using the notation introduced by Stokes *et al*. [28]. Local- and average-distortion patterns are indicated using plain (in parenthesis) and bold letters, respectively. The solid (black) line corresponds to the transition temperatures determined by fitting a sigmoidal function to the XRD data; light-gray regions associated with this line reflect the width of the transitions as determined by the ΔT values obtained from the sigmoidal fits. The line (dashed/blue) of the in-phase tilting transition should be considered as approximate. The transition line (dashed/black) that delineates a stability field for the high-temperature NBT-like tetragonal phase is hypothetical and has yet to be established experimentally. The coherence length for the in-phase tilting is limited to the nanoscale outside of this field. The dashed green line signifies the ferroelectric transition, which for $0 \leq x \leq 0.1$ appears to occur below the tilting transition.

Fig. 13: Temperature dependence for widths of characteristic XRD peaks (laboratory data) used to estimate temperatures of phase transitions. The diffraction data for x=0.15 and x=0.25 were measured using a laboratory diffractometer, whereas the data for x=0.2 were obtained using synchrotron radiation. In all cases, peaks were fitted using a 4-parameter Pearson VII function. The error bars correspond to standard uncertainties due to profile fitting. For x=0.15 and x=0.25, the uncertainties are smaller than the symbol size. For x=0.2 an integral breadth was used instead of a full-width-at-half-maximum (FWHM) to reduce the noise in the data. For x=0.15 and x=0.25, the results for both heating (red) and cooling (blue) are shown. In both cases, a small but reproducible hysteresis is observed. The dashed lines passing through red symbols in the plots for x=0.15 and x=0.25 represent fits using a sigmoidal function. The arrow in the plot for x=0.2 indicates an anomaly in the slope, which is attributed to the phase transition.

Fig. 14: Temperature dependence for (a) widths of 110 and 200, (b) asymmetry of 111 peak, and (c) integrated intensities of ½311 and ½310 superlattice reflections in NBT, as measured using XRD (laboratory data). Temperatures of the structural phase transitions are indicated using dashed gray lines. The depolarization temperature, determined from dielectric measurements, is indicated using a dashed orange line.

Fig. 15: Temperature dependence of dielectric constant and losses for a series of *unpoled* NBT-KBT compositions. Different measurement frequencies are indicated using color: black –

0.1 kHz, red – 1 kHz, blue – 10 kHz, orange – 100 kHz, and green – 1000 kHz. The direction of increasing frequency is additionally indicated using a dashed-line arrow in the plot for x=0. All samples exhibit a broad maximum around 300 °C and another anomaly at lower temperatures. The lower temperature anomaly (indicated using a dashed gray line in the plot for x=0.1) has been attributed to a ferroelectric transition. The spread of this anomaly correlates with a spread of the corresponding phase transition seen in Fig. 12. The structural origin of the high-temperature dielectric peak remains unclear.

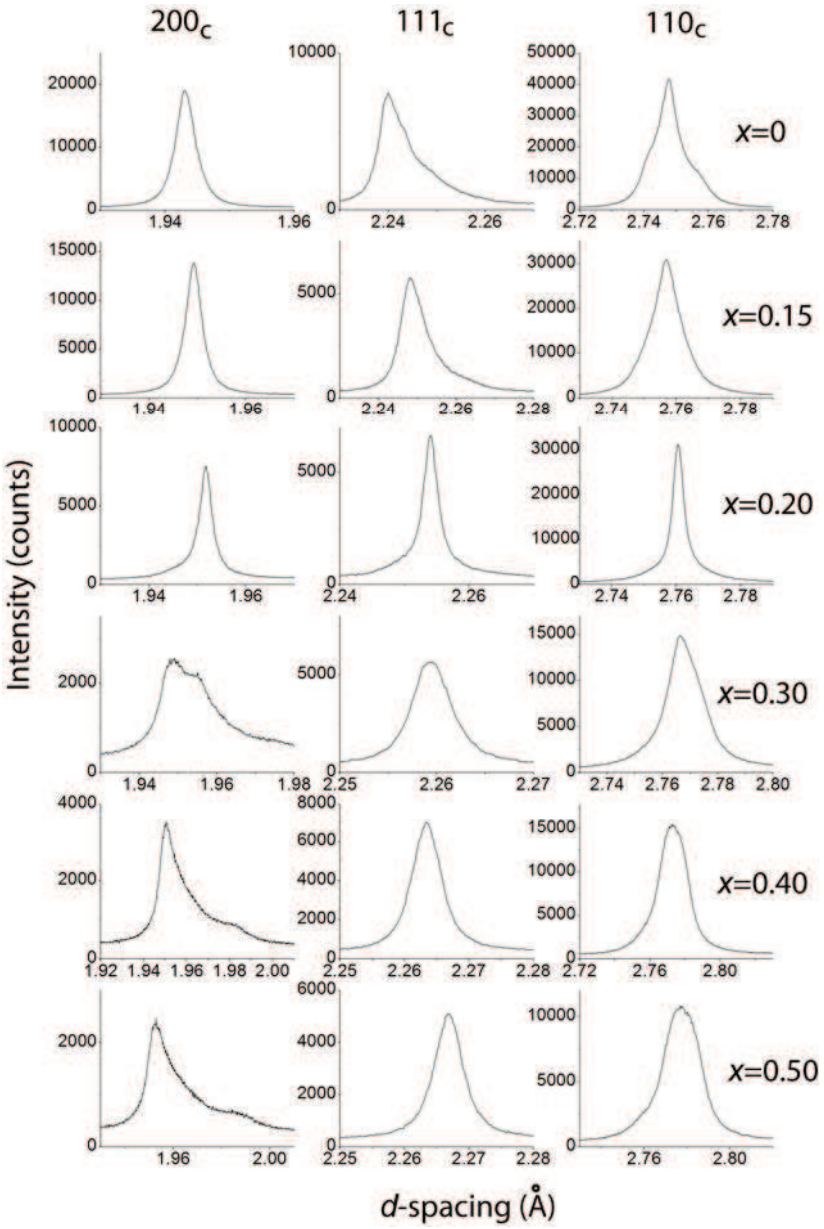

Figure 1 BT12212 14JAN2013

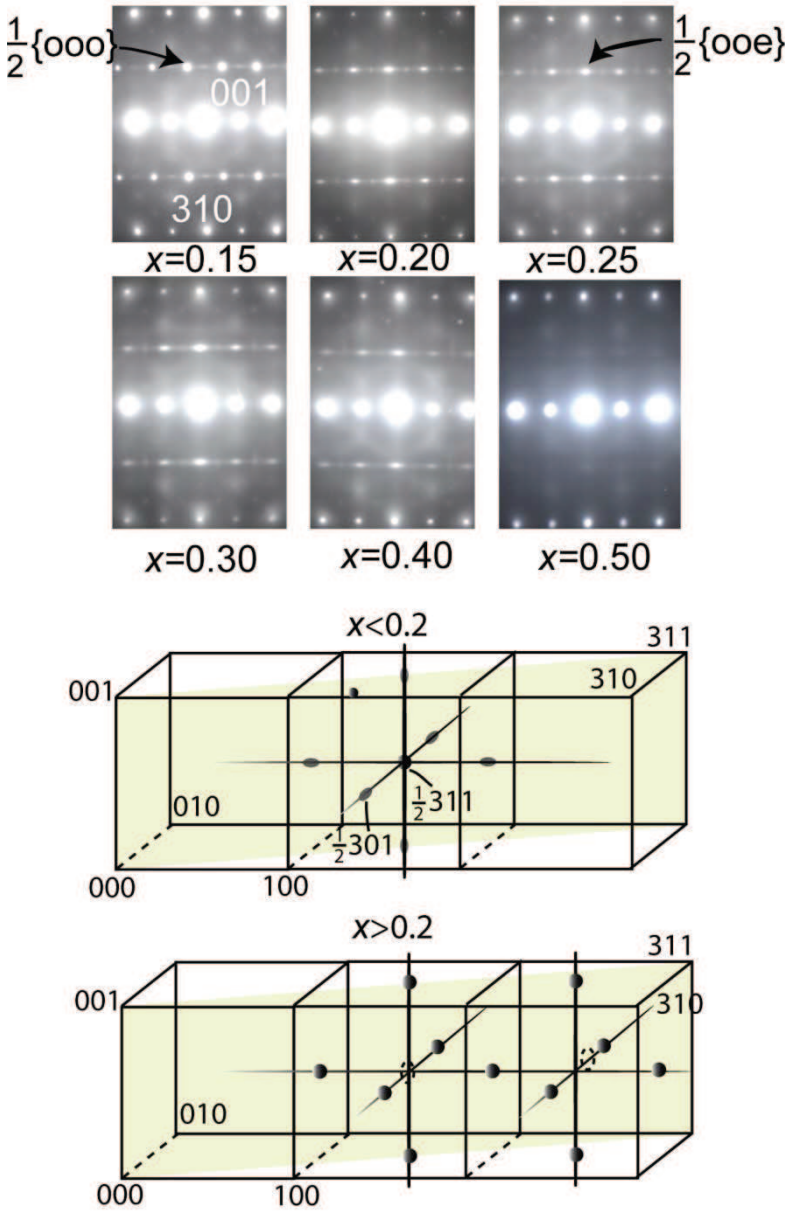

Figure 2 BT12212 14JAN2013

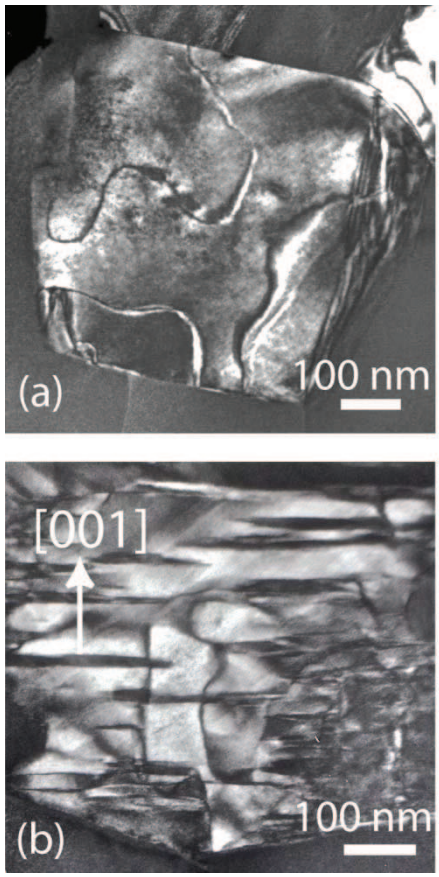

Figure 3 BT12212 14JAN2013

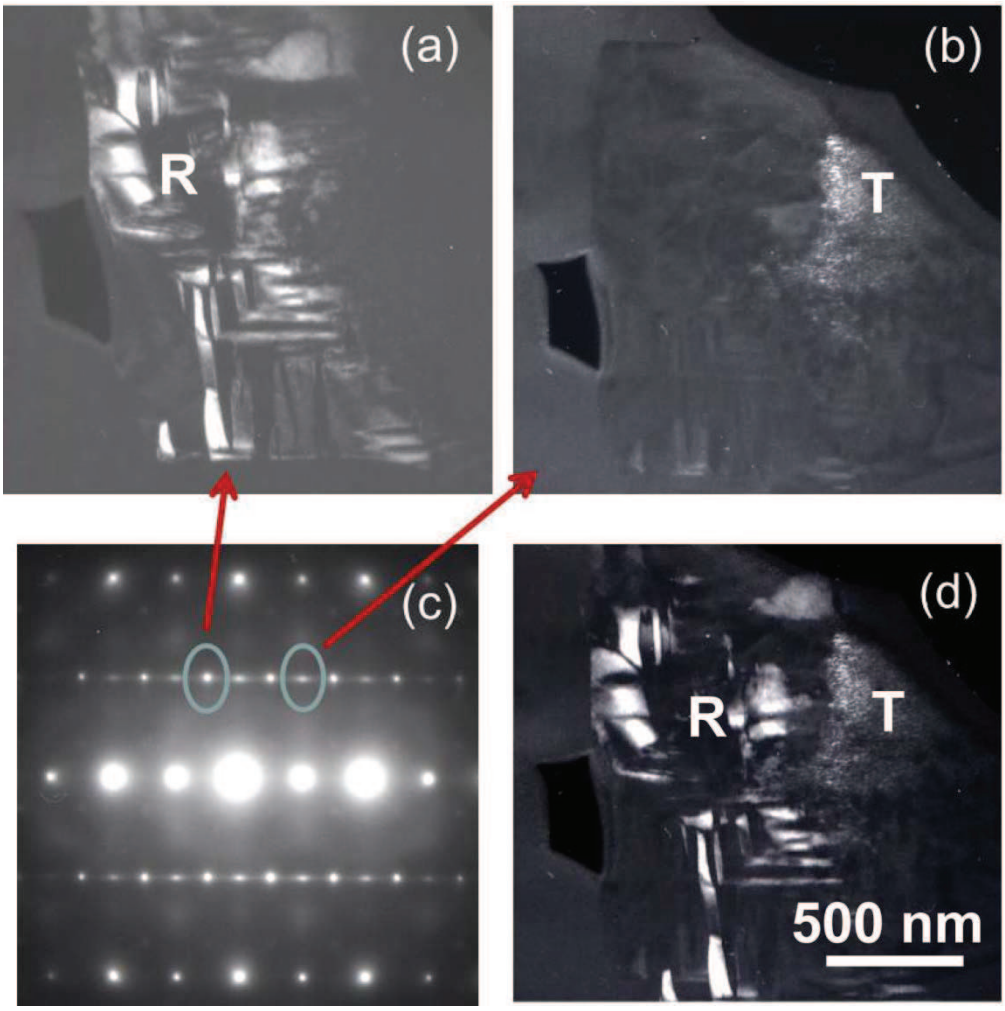

Figure 4 BT12212 14JAN2013

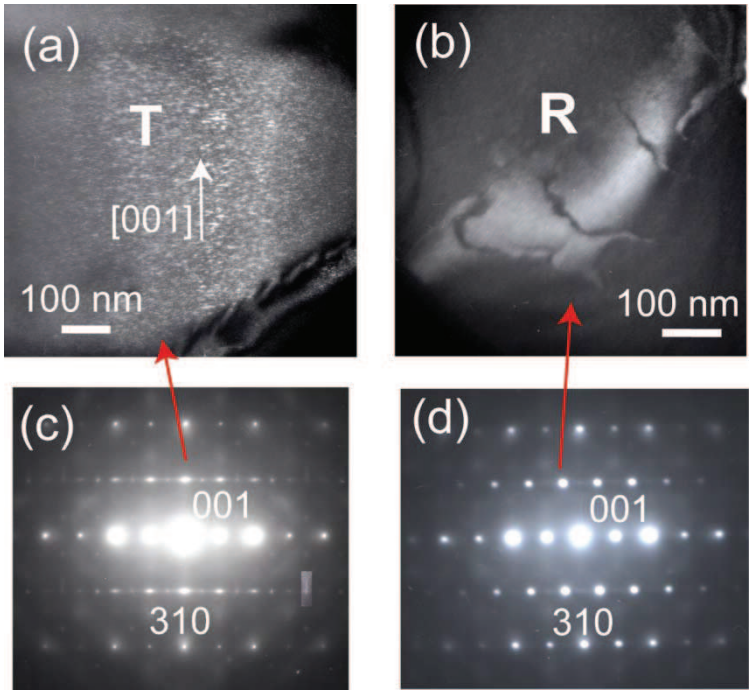

Figure 5 BT12212 14JAN2013

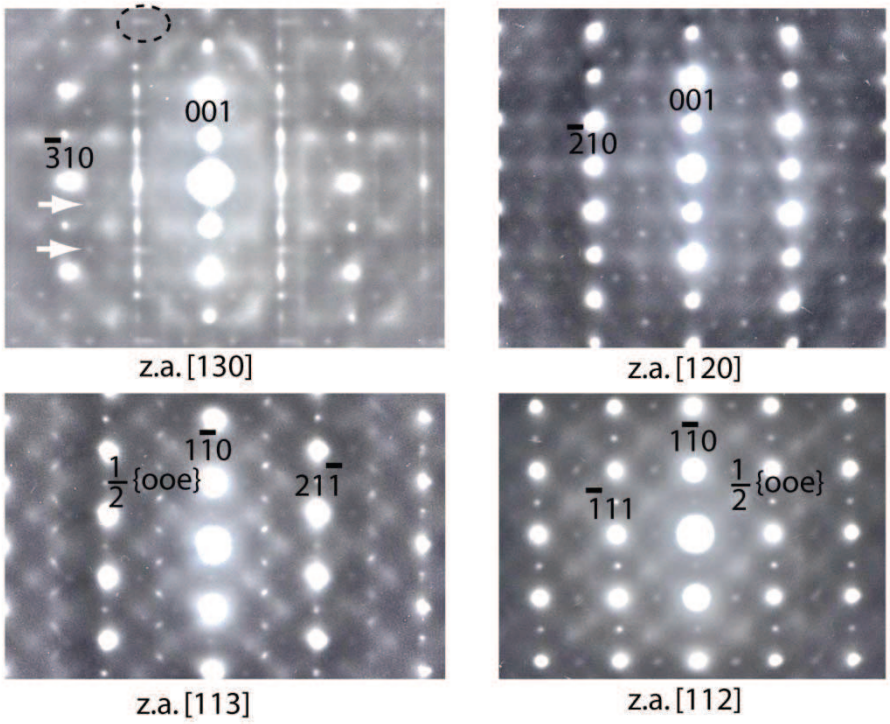

Figure 6 BT12212 14JAN2013

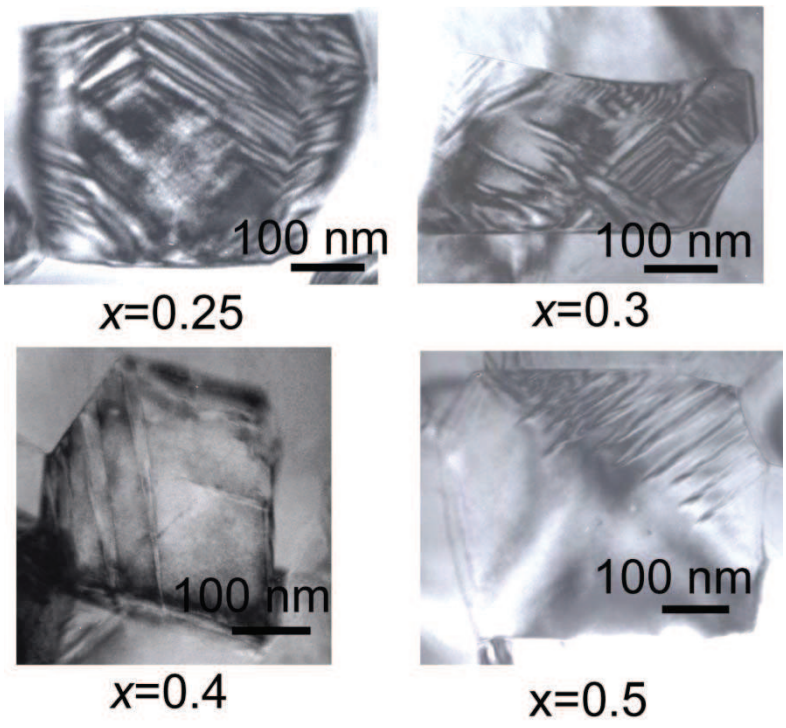

Figure 7 BT12212 14JAN2013

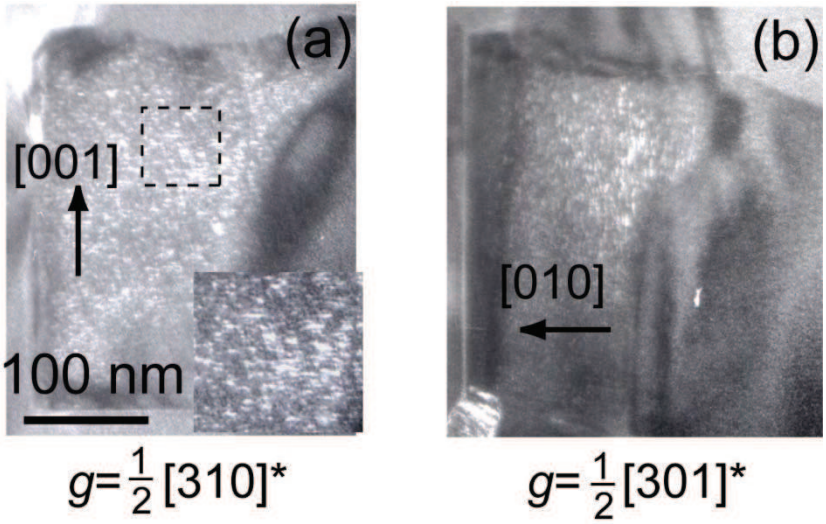

Figure 8 BT12212 14JAN2013

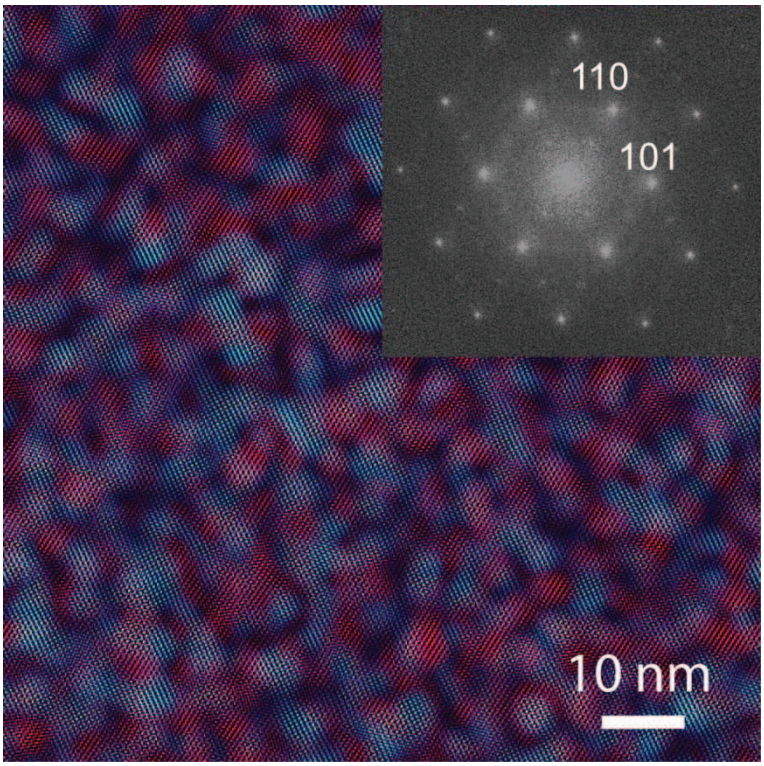

Figure 9 BT12212 14JAN2013

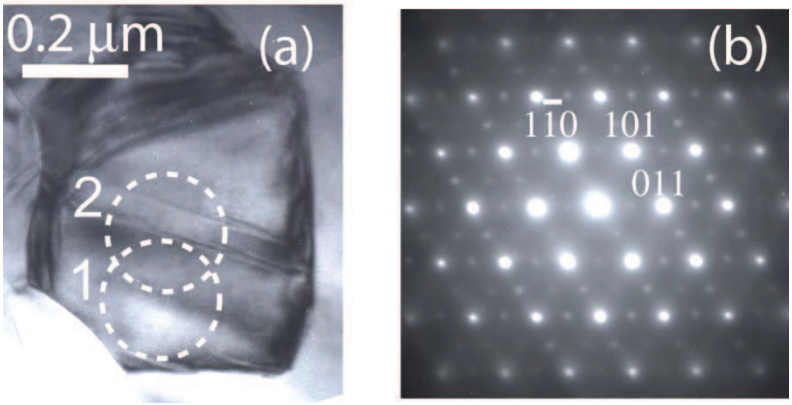

Figure 10 BT12212 14JAN2013

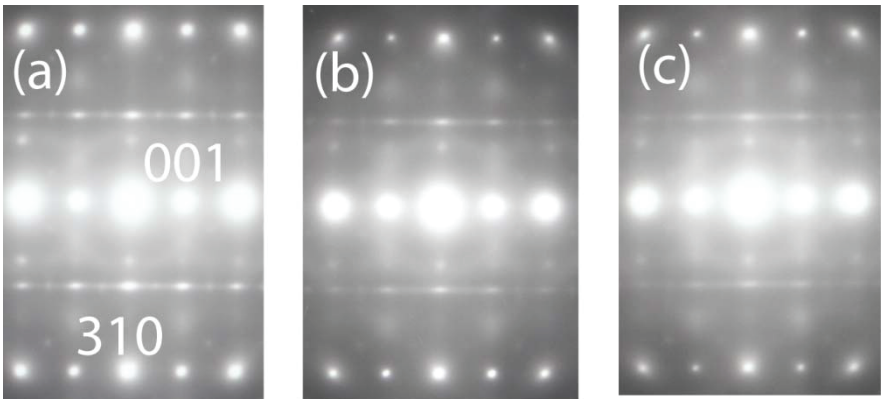

Figure 11 BT12212 14JAN2013

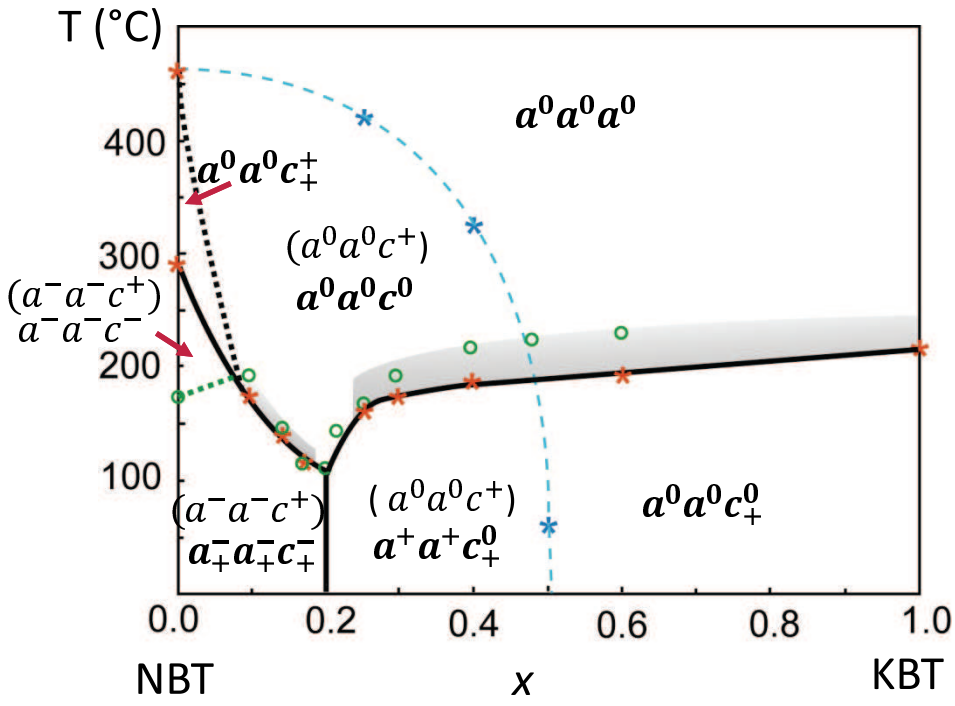

Figure 12 BT12212 14JAN2013

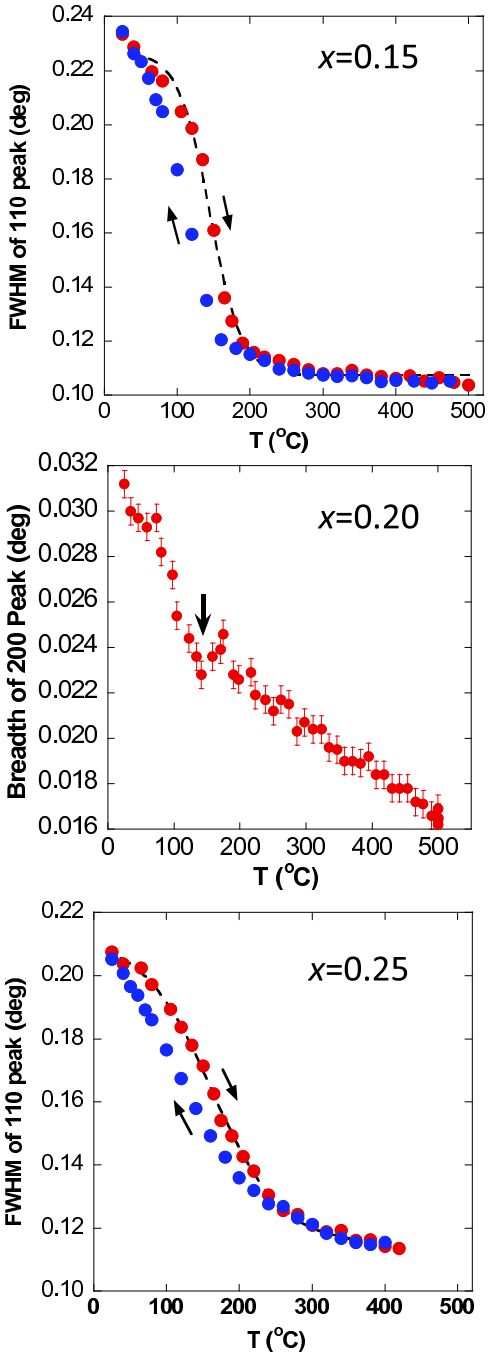

Figure 13 BT12212 14JAN2013

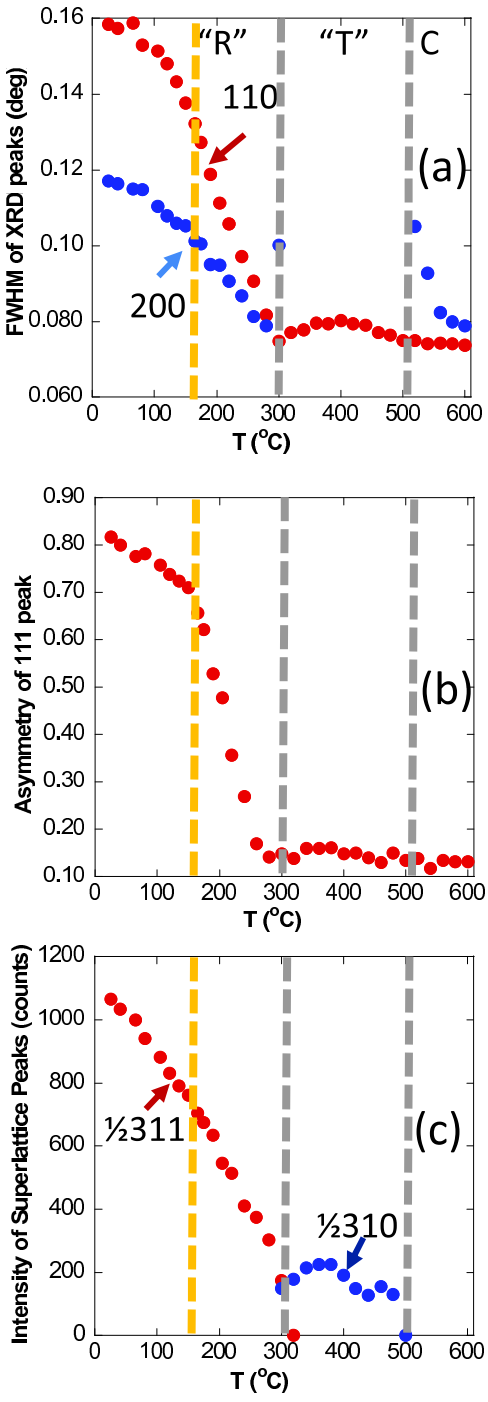

Figure 14 BT12212 14JAN2013

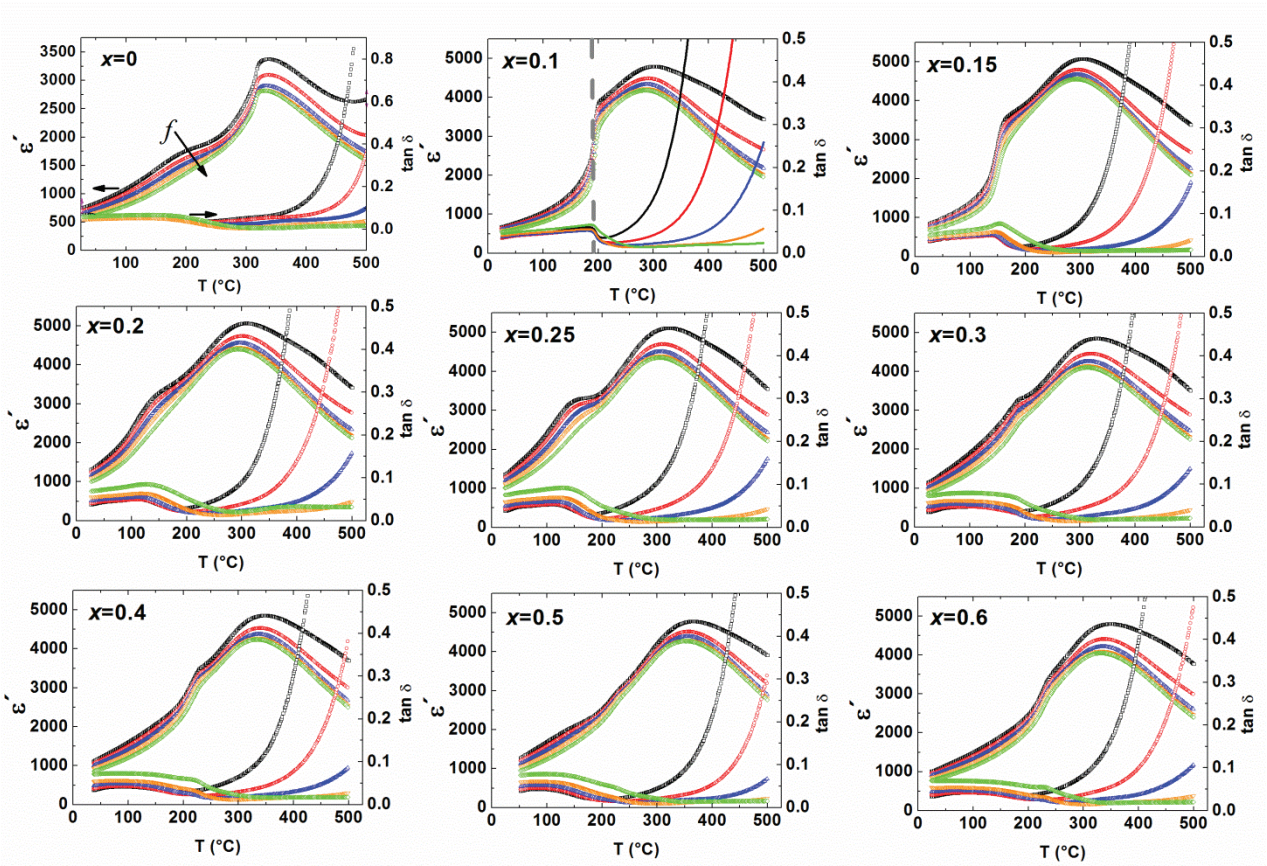

Figure 15 BT12212 14JAN2013